

SCIENTIFIC REPORTS



OPEN

Significant improvement in Mn_2O_3 transition metal oxide electrical conductivity via high pressure

Fang Hong^{1,2}, Binbin Yue^{1,2}, Naohisa Hirao³, Zhenxian Liu⁴ & Bin Chen¹

Received: 25 October 2016

Accepted: 02 February 2017

Published: 09 March 2017

Highly efficient energy storage is in high demand for next-generation clean energy applications. As a promising energy storage material, the application of Mn_2O_3 is limited due to its poor electrical conductivity. Here, high-pressure techniques enhanced the electrical conductivity of Mn_2O_3 significantly. *In situ* synchrotron micro X-Ray diffraction, Raman spectroscopy and resistivity measurement revealed that resistivity decreased with pressure and dramatically dropped near the phase transition. At the highest pressure, resistivity reduced by five orders of magnitude and the sample showed metal-like behavior. More importantly, resistivity remained much lower than its original value, even when the pressure was fully released. This work provides a new method to enhance the electronic properties of Mn_2O_3 using high-pressure treatment, benefiting its applications in energy-related fields.

Transition metal oxides have unique properties that are capable of developing new, functional and smart materials. In particular, manganese oxide has been a key focus due to its outstanding structural diversity and novel physicochemical properties^{1–4}. It also has the advantage of being earth abundant, non-toxic and cost effective, attracting enormous attention for a wide variety of energy and environmental applications, such as chemical catalysts, magnetic devices, and energy conversion and storage^{5–10}. Mn_2O_3 is a semiconductor but it can be employed as a high-performance anode material in Lithium-ion batteries (LIBs), with a high theoretical capacity of 1018 mAh/g at a low operating voltage (charge voltage at 1.2 V and discharge voltage at 0.5 V)¹¹. Furthermore, its one electron transfer caused by electrochemical redox activity via the Mn^{3+} to Mn^{4+} transition is significant for its electrode reactions in electrochemical capacitors.

Electrode materials for batteries and supercapacitors must have good electrical conductivity to achieve high electrochemical performance^{12,13}. Poor electrical conductivity may limit the solid-state diffusion rate of the electrons and/or ions, consequently resulting in reduced power and energy density. In this regard, the poor electrical conductivity of Mn_2O_3 is a major drawback. Traditionally, the electrical conductivity of transition metal oxides can be enhanced by forming nanocomposite materials with highly conductive carbon or graphene. Alternatively, cationic doping achieves a similar effect^{14,15}. In addition, various nanostructures like nanorods, nanospheres, and mesoporous Mn_2O_3 have been prepared and demonstrate a clear improvement in the specific capacitance^{16–18}. These methods have undoubtedly boosted the development of transition metal oxide-based energy storage. However, sometimes these methods have additional problems, such as low thermal stability and an increased manufacturing cost. Therefore, improving the intrinsic electrical conductivity of transition metal oxides for high-performance energy storage is imperative. Recent works have shown pressured-induced electron transport enhancement of Nb-doped TiO_2 nanoparticles and single-crystal Ta_2O_5 nanowires^{19,20} and there are further reports of pressure-induced superconductivities^{21,22}. Therefore, pressure may be a powerful tool to modify the electrical conductivity of transition metal oxides.

Here, we tentatively studied the electrical properties of the promising transition metal oxide, Mn_2O_3 , using high-pressure to reveal the relationship between its electrical properties and structure. First, we investigated the electrical properties *in situ* inside a diamond anvil cell by resistance measurements at room temperature and pressures up to 43 GPa. The electrical conductivity enhanced by five orders of magnitude at the highest pressure. More importantly, conductivity after high-pressure treatment was more than ten times higher than the original level before treatment at ambient conditions. To reveal the mechanism of this enhancement behavior, we examined the

¹Center for High Pressure Science and Technology Advanced Research, 1690 Cailun Rd. Pudong, Shanghai 201203, P.R. China. ²The Advanced Light Source, Lawrence Berkeley National Laboratory, 1 Cyclotron Rd, Berkeley, CA 94720, USA. ³Spring-8/JASRI, 1-1-1 Kouto, Sayo-cho, Sayo-gun, Hyogo 679-5198, Japan. ⁴Geophysical Laboratory, Carnegie Institution of Washington, Washington, DC 20015, USA. Correspondence and requests for materials should be addressed to B.Y. (email: byue@lbl.gov) or B.C. (email: chenbin@hpstar.ac.cn)

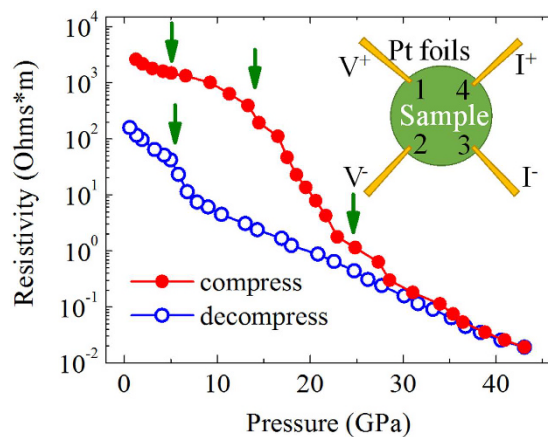


Figure 1. The pressure dependent resistivity of Mn_2O_3 during compression and decompression. Insert: the scheme of electrical measurements in the diamond anvil cell.

structural evolution of Mn_2O_3 under high pressure using *in situ* synchrotron x-ray diffraction (XRD) and Raman spectroscopy at room temperature; a phase transition began around 18.5 GPa and 15 GPa, respectively. We also examined the electronic structure by infrared spectroscopy and proved that Mn_2O_3 behaves like a metal rather than a semiconductor under high pressure. This work provides an efficient way to improve the electrical conductivity of manganese oxides, benefiting their applications as electrode materials for high-performance batteries and supercapacitors.

Results and Discussion

The electrical measurement of Mn_2O_3 under high pressure. Figure 1 displays the pressure dependent electrical resistivity of Mn_2O_3 during both compression and decompression. During compression, resistivity shows a clear decreasing trend with increasing pressure and a huge resistivity drop occurs. At the highest pressure of ~ 43 GPa, the resistivity is only on the scale of $\sim 10^{-2}$ Ohms*m compared to $\sim 10^3$ Ohms*m near ambient conditions. A sharp resistivity change from ~ 15 GPa to ~ 25 GPa indicates an electronic transition. In addition, a minor kink near 5 GPa may also suggest an electronic transition. This transition is much clearer when the resistivity-pressure curve is plotted on a linear scale, as shown in Figure S1 in the Supplementary information. During decompression, the pressure dependent resistivity trend is the opposite. It increases with pressure release and a kink appears near 5 GPa, which may be related to an inverse electronic transition. When pressure is fully released, resistivity remains one order of magnitude lower than it was before compression.

Interestingly, the relationship between resistivity and pressure can be well described by a logarithmic function for each phase. To exclude the grain boundary effect and mixed phases, we only fitted the decompression data with logarithmic functions. The fitting details are provided in Figure S2 in the Supplementary information. The pressure dependent resistivity can be expressed by the following relationship:

For the high-pressure range:

$$\ln \rho = 3.38 - 0.17P \quad (1)$$

For the low-pressure range:

$$\ln \rho = 5.16 - 0.29P \quad (2)$$

where ρ is the resistivity and P is the pressure. Similar logarithmic behavior of pressure dependent resistivity has also been found in VO_2 , MoSe_2 , and GeSb_2Te_4 .^{23–25}

The crystal structure investigated by synchrotron x-ray diffraction and Raman spectroscopy under high pressure.

To understand the mechanism of the enhanced electrical conductivity, we examined the Mn_2O_3 structural evolution under high pressure. Figure 2 demonstrates the X-ray diffraction patterns at various pressures during compression. At low pressure, the structure of Mn_2O_3 can be well assigned to a cubic phase with the $Ia-3$ space group²⁶. New diffraction peaks appear clearly from 18.5 GPa, suggesting that a phase transition has already occurred. The new phase mixes with the cubic phase from 18.5 GPa to 26.5 GPa before the cubic phase is completely suppressed above 26.5 GPa. This high-pressure phase can be assigned to an orthorhombic structure with the space group $Cmcm$ ²⁶. Figure 2(b,c) shows representative refinement patterns of Mn_2O_3 collected at 34.4 GPa and 1.6 GPa, corresponding to the high-pressure orthorhombic phase and the low-pressure cubic phase, respectively. The refinement merit is indicated by the Rwp values, which are quite small at only 1.75% and 2.04%. The structural details of these two pressure points are listed in Table S1 in the Supplementary information.

The pressure dependent structural information is presented in Fig. 3. Figure 3(a) displays the pressure dependent lattice parameters. For the cubic phase, the lattice parameter decreases monotonously with pressure. For the orthorhombic phase, the a axis shows a clear declining trend with pressure, while the c axis shows little change and the b axis decreases slowly above the final phase transition pressure of 26.5 GPa. Figure 3(b) demonstrates the volume

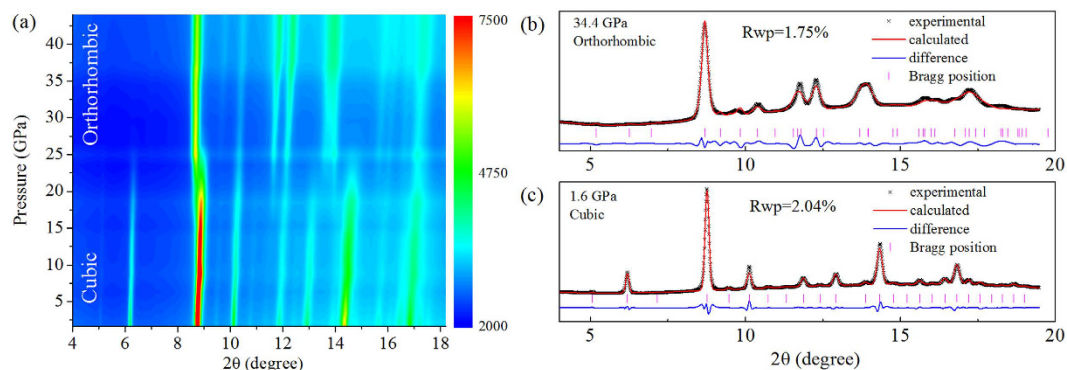


Figure 2. The X-ray diffraction results of Mn_2O_3 up to ~ 44 GPa (wavelength is 0.4141 \AA) during compression. (a) Two-dimensional X-ray diffraction patterns. (b,c) The representative refinement patterns at 34.4 GPa and 1.6 GPa, respectively. A structural phase transition is observed near 18 GPa and finishes near 26.5 GPa. The refinement merit is indicated by the Rwp values, which are very small.

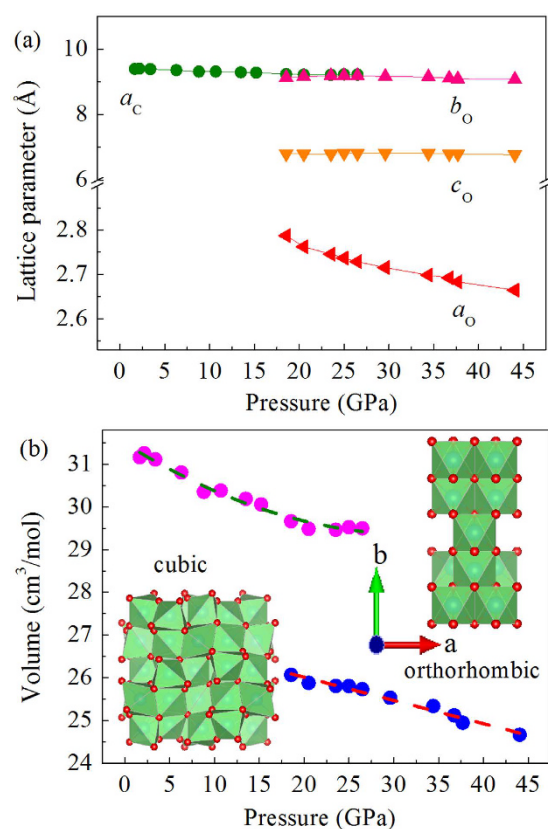


Figure 3. Refinement results of Mn_2O_3 structural information during compression. (a) The pressure dependent lattice parameters. (b) Volume evolution under high pressure (inset: atomic structures of cubic and orthorhombic phases). There is a large volume collapse at the phase transition pressure. At ~ 18.5 GPa, the volume difference of the two phases reaches $\sim 12\%$.

evolution with pressure; the large change in the atomic structure causes a significant volume change near the phase transition pressure. The unit volume of the orthorhombic structure at 18.5 GPa is only $\sim 87.5\%$ of the cubic structure. In the high-pressure orthorhombic structure, oxygen atoms in the ab -plane show a highly ordered arrangement and the MnO_6 units are less distorted compared to those in the cubic structure, as demonstrated by the insets in Fig. 3(b). Large pressure-induced volume changes in transition metal compounds are usually related to an electronic structural change of the transition metal ions (such as Fe, Co, and Mn), which can undergo a spin state transition from a high/intermediate spin state to a low spin state^{27–29}. The spin state transition of MnS_2 has a volume collapse as large as 22% from the low-pressure cubic structure to a high-pressure monoclinic structure near 18 GPa. Recently, a spin state transition was also observed in MnS and MnSe with a large volume collapse³⁰. Here, the large volume collapse in our Mn_2O_3 may originate from a spin state transition too but further study is required to clarify this assumption.

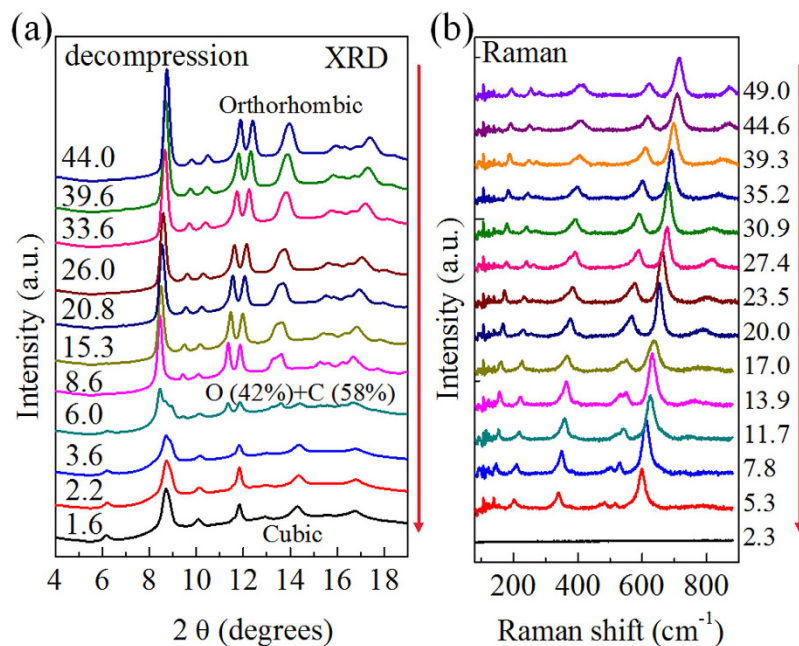


Figure 4. Structural investigation during decompression. (a) Pressure dependent X-ray diffraction patterns. (b) Pressure dependent Raman spectra. Pressure unit: GPa.

We also investigated the Mn_2O_3 structural evolution by Raman spectroscopy during compression. The results are provided in Figure S3 in the Supplementary information. A structural phase transition occurred near 15 GPa, indicated by two new, strong vibration modes (~ 550 and ~ 650 cm^{-1} at 20 GPa). Two extra modes located at ~ 150 and ~ 200 cm^{-1} became more pronounced when the pressure reached ~ 18 GPa, suggesting an overall phase transition occurred. This is well consistent with the XRD results and no further change was observed in the current pressure limit. The Raman spectra results confirmed that the structural phase transition started ~ 15 GPa, a little bit lower than the XRD result determination. The phase transition also matched the resistivity measurement.

We studied the compressibility of the Mn_2O_3 low-pressure (cubic) and high-pressure (orthorhombic) structures using second-order Birch-Murnaghan equation of state (EOS) analysis^{31,32}. The fitting results are presented in Figure S4 in the Supplementary information. For the cubic phase, V_0 is 34.43 cm^3/mol and the bulk modulus B_0 is 286.4 ± 16.6 GPa, using a fixed first-order pressure derivative of the bulk modulus $B' = 4$. For the orthorhombic phase, V_0 is 27.5 cm^3/mol and the bulk modulus B_0 is 331.09 ± 28.3 GPa, using a fixed first-order pressure derivative of the bulk modulus $B' = 4$. Hence, the high-pressure phase is a little more difficult to compress than the low-pressure phase.

To reveal the mechanism of the different electrical resistivity behavior under compression and decompression, XRD and Raman spectra were also collected during decompression, as shown in Fig. 4(a and b), respectively. No phase transition occurred when the pressure was released to 8.6 GPa, as confirmed by our XRD results. However, a clear difference was visible near 6.0 GPa, where an extra diffraction peak appeared. Subsequently, the low-pressure phase dominated and we assigned this phase to the previous cubic phase, though the peaks broadened and the intensity of some peaks was lower, compared with those during compression. The broadening and intensity changes were due mainly to the reduced crystal size and disorders induced by pressure. The Raman spectra gave similar results. No clear change presented until pressure reduced to 5.3 GPa. After that, the intensity of the Raman signal almost disappeared and no peaks were identified. This was consistent with the cubic phase, where the Raman signal was much weaker than in the orthorhombic phase. The disorders and smaller crystal size also affect the Raman signal in the low-pressure range, which made the weak Raman signal much more difficult to collect. These results match well with previous reports of high-pressure phase stability until 4.5 GPa during decompression^{33,34}. More importantly, the structural change during decompression and the resistance measurement results are also consistent, as displayed in Fig. 1. Hence, the electronic transition near 5 GPa originates from a reversible structural phase transition. Similar results have been reported on other materials²⁰. The microstructural change after high-pressure treatment should be responsible for the enhanced conductivity behavior. Pressure can drive lattice distortion and even slip^{35,36}, during which defects appear, breaking the original locally neutral charge distribution and aiding electron transfer.

Infrared spectroscopy study on Mn_2O_3 under high pressure. The electronic behavior of Mn_2O_3 under high pressure was investigated by synchrotron-based infrared spectroscopy (IR) to reveal the electronic structural change. Figure 5 presents the reflectivity spectra at some typical pressures. As the sample we used in the IR measurement was a fine powder, the reflectivity signal was noisy and relatively low due to strong scattering on the coarse surface. However, we still observed a clear trend under high pressure, which helps us understand its electronic behavior. An average dot plot for each spectrum guides the eyes. We expected the spectrum at 2.0 GPa to be similar to that at ambient conditions. It shows typical reflective behavior from a semiconductor or insulator,

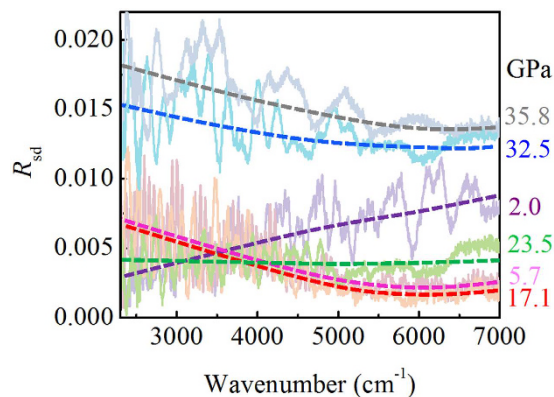


Figure 5. The IR reflectance spectroscopy of Mn_2O_3 under high pressure. Some changes at certain pressures (5.7 GPa, 23.5 GPa, 32.5 GPa) indicate electronic structural changes.

where reflectance is lower in a low wave number (low-energy) region than in a high wave number (high-energy) region. No obvious change occurred when the pressure increased a little from 2.0 GPa to 3.7 GPa (shown in Figure S5(a) in the Supplementary information). The trend suddenly changed at 5.7 GPa, which is characteristic of metal-like behavior as reflectance is higher in the low wave number region than in the high wave number region. This is also consistent with the resistance measurement result during compression in Fig. 1, where a kink occurs near 5 GPa. This change suggests that a previously unreported electronic phase transition occurred near 5 GPa. Above 5.7 GPa, the reflectance slightly increased with pressure in the long wavenumber range (shown in Supplementary information Figure S5(b)), suggesting better conductivity and metal-like behavior. This trend changed when the pressure reached 17.1 GPa, near the structural phase transition. The reflectance decreased at 17.1 GPa to even lower than at 5.7 GPa. Another change occurred between 23.5 GPa and 26.7 GPa where reflectance strengthened due to the completion of the structural phase transition. Figure 5 shows stronger reflection at 32.5 GPa or higher pressure, and this trend follows a metal-like behavior. To briefly summarize the observed electronic behavior; the sample underwent an electronic phase transition near 5.7 GPa with no structural change and a structural phase transition induced electronic structure change near 17.1 GPa. The phase transition concluded between 23.5 and 26.7 GPa. These IR results agree with the resistance measurements and structural analysis.

Conclusion

In summary, we systematically investigated the electronic and structural properties of Mn_2O_3 under high pressure using resistivity measurements, X-ray diffraction, Raman spectroscopy, and infrared spectroscopy. A cubic-orthorhombic phase transition began near 15.1 GPa. The resistivity dropped sharply near this transition and the sample showed some metal-like features at higher pressure. Clearly, high pressure strongly enhanced electrical conductivity. The quenched sample maintained better electrical conductivity than its original value. Our work helps solve the problem of poor Mn_2O_3 electrical conductivity without the addition of another element, allowing wider applications in the energy storage field.

Methods

High-pressure XRD, Raman, and IR study at room temperature. The $\alpha\text{-Mn}_2\text{O}_3$ (99.99% trace metals basis) was purchased from Sigma-Aldrich. *In situ* Raman spectra and X-ray diffraction patterns under various pressures were collected from the $\alpha\text{-Mn}_2\text{O}_3$ sample, which was loaded into a Mao-type symmetric diamond anvil cell (DAC) with a diamond culet of $300\ \mu\text{m}$ ^{37,38}. Silicone oil was used as a pressure medium. Reports suggest that silicone oil hydrostaticity is as good as a 4:1 methanol:ethanol mixture at low pressures to ~ 20 GPa and behaves like argon above 30 GPa^{39,40}. The Raman spectra were collected using a micro-confocal Renishaw Raman system with a 532 nm green laser³⁸. A stainless steel gasket was used and a $100\ \mu\text{m}$ sample hole was drilled with a laser drilling system. The pressure was monitored by the Ruby R1-R2 line shift. The *in situ* synchrotron micro X-ray diffraction experiment was carried out at Beamline 10XU in Spring-8 and the incident X-ray wavelength was $0.4142\ \text{\AA}$. The patterns were collected using a Perkin Elmer digital X-ray flat panel detector (FPD, XRD0822 CP23; 1024×1024 pixels; $0.2\ \text{mm}$ pixel pitch). Infrared spectra were collected *in situ* inside the DAC using IR diamonds at Beamline 1.4.4 in the Advanced Light Source at Lawrence Berkeley National Laboratory, using KBr as the pressure medium.

High-pressure electrical resistivity measurements at room temperature. *In situ* high-pressure electrical resistance measurements were conducted with a four-probe resistance test system in a DAC at pressures up to 43.09 GPa. The mixture of boron nitride (BN) and epoxy was loaded between the sample and the gasket to provide an electrical insulation layer. The other parts of the gasket were covered with insulating glue to avoid contact between the conductive leads and metal gasket. The sample was loaded into the BN hole without a pressure medium. Four platinum foils were arranged to contact the sample in the chamber. A Keithley 6221 current source and 2182A nano-voltmeter were used as the current supply and voltmeter, respectively. The resistance was determined by the Van de Pauw method, similar to that described in reference⁴¹.

References

- Ovsyannikov, S. V. *et al.* Perovskite-like Mn_2O_3 : A Path to New Manganites. *Angew. Chem. Int. Ed.* **52**, 1494–1498 (2013).
- Kuo, C.-H. *et al.* Understanding the Role of Gold Nanoparticles in Enhancing the Catalytic Activity of Manganese Oxides in Water Oxidation Reactions. *Angew. Chem. Int. Ed.* **54**, 2345–2350 (2015).
- Ovsyannikov, S. V. *et al.* Perovskites: A Hard Oxide Semiconductor with A Direct and Narrow Bandgap and Switchable p–n Electrical Conduction. *Adv. Mater.* **26**, 8184 (2014).
- Williams, K. S. *et al.* Magnetic structure variation in manganese-oxide clusters. *The Journal of Chemical Physics* **136**, 134315 (2012).
- Jagadeesh, R. V. *et al.* Nanoscale Fe_2O_3 -Based Catalysts for Selective Hydrogenation of Nitroarenes to Anilines. *Science* **342**, 1073–1076 (2013).
- Liao, L. *et al.* Efficient solar water-splitting using a nanocrystalline CoO photocatalyst. *Nature Nano.* **9**, 69–73 (2014).
- Chen, Y. S. *et al.* Anticrossstalk characteristics correlated with the set process for $\alpha\text{-Fe}_2\text{O}_3/\text{Nb-SrTiO}_3$ stack-based resistive switching device. *Appl. Phys. Lett.* **97**, 262112 (2010).
- Zhong, D. K., Sun, J., Inumaru, H. & Gamelin, D. R. Solar Water Oxidation by Composite Catalyst/ $\alpha\text{-Fe}_2\text{O}_3$ Photoanodes. *J. Am. Chem. Soc.* **131**, 6086–6087 (2009).
- Fekete, M. *et al.* Highly active screen-printed electrocatalysts for water oxidation based on [small beta]-manganese oxide. *Energy Environ. Sci.* **6**, 2222–2232 (2013).
- Yang, M. K., Kim, G. H., Ju, H., Lee, J.-K. & Ryu, H.-C. The interfacial layer effect on bi-stable resistive switching phenomenon in MnO_2 thin film. *Appl. Phys. Lett.* **107**, 053503 (2015).
- Qiu, Y. *et al.* Morphology-conserved transformation: synthesis of hierarchical mesoporous nanostructures of Mn_2O_3 and the nanostructural effects on Li-ion insertion/deinsertion properties. *J. Mater. Chem.* **21**, 6346–6353 (2011).
- Hall, P. J. *et al.* Energy storage in electrochemical capacitors: designing functional materials to improve performance. *Energy Environ. Sci.* **3**, 1238–1251 (2010).
- Wei, W., Cui, X., Chen, W. & Ivey, D. G. Manganese oxide-based materials as electrochemical supercapacitor electrodes. *Chem. Soc. Rev.* **40**, 1697–1721 (2011).
- Li, Q. *et al.* Copper Doped Hollow Structured Manganese Oxide Mesocrystals with Controlled Phase Structure and Morphology as Anode Materials for Lithium Ion Battery with Improved Electrochemical Performance. *ACS Appl. Mater. Interfaces* **5**, 10975–10984 (2013).
- Jiang, H. *et al.* High-rate electrochemical capacitors from highly graphitic carbon-tipped manganese oxide/mesoporous carbon/manganese oxide hybrid nanowires. *Energy Environ. Sci.* **4**, 1813–1819 (2011).
- Deng, Y., Wan, L., Xie, Y., Qin, X. & Chen, G. Recent advances in Mn-based oxides as anode materials for lithium ion batteries. *RSC Adv.* **4**, 23914–23935 (2014).
- Ji, L., Lin, Z., Alcoutlabi, M. & Zhang, X. Recent developments in nanostructured anode materials for rechargeable lithium-ion batteries. *Energy Environ. Sci.* **4**, 2682–2699 (2011).
- Wang, Y. *et al.* All-Nanowire Based Li-Ion Full Cells Using Homologous Mn_2O_3 and LiMn_2O_4 . *Nano Letters* **14**, 1080–1084 (2014).
- Lü, X. *et al.* Enhanced Electron Transport in Nb-Doped TiO_2 Nanoparticles via Pressure-Induced Phase Transitions. *J. Am. Chem. Soc.* **136**, 419–426 (2014).
- Lü, X. *et al.* Pressure-Induced Amorphization in Single-Crystal Ta_2O_5 Nanowires: A Kinetic Mechanism and Improved Electrical Conductivity. *J. Am. Chem. Soc.* **135**, 13947–13953 (2013).
- Drozdov, A. P., Erements, M. I., Troyan, I. A., Ksenofontov, V. & Shylin, S. I. Conventional superconductivity at 203 kelvin at high pressures in the sulfur hydride system. *Nature* **525**, 73–76 (2015).
- Takahashi, H. *et al.* Pressure-induced superconductivity in the iron-based ladder material BaFe_2S_3 . *Nat Mater* **14**, 1008–1012 (2015).
- Zhang, X. *et al.* Anomalous semiconducting behavior on VO_2 under high pressure. *RSC Advances* **5**, 54843–54847 (2015).
- Xu, M., Yu, Z., Wang, L., Mazzarello, R. & Wuttig, M. Reversing the Resistivity Contrast in the Phase-Change Memory Material GeSb_2Te_4 Using High Pressure. *Adv. Electron. Mater.* **1**, 1500240 (2015).
- Zhao, Z. *et al.* Pressure induced metallization with absence of structural transition in layered molybdenum diselenide. *Nature Commun.* **6**, 7312 (2015).
- Santillán, J., Shim, S.-H., Shen, G. & Prakapenka, V. B. High-pressure phase transition in Mn_2O_3 : Application for the crystal structure and preferred orientation of the CaIrO_3 type. *Geophys. Res. Lett.* **33**, 026423 (2006).
- Lin, J.-F. *et al.* Spin Transition Zone in Earth's Lower Mantle. *Science* **317**, 1740–1743 (2007).
- Lin, J.-F. *et al.* Spin transition of iron in magnesiowüstite in the Earth's lower mantle. *Nature* **436**, 377–380 (2005).
- Lin, J.-F., Speziale, S., Mao, Z. & Marquardt, H. Effects of the electronic spin transitions of iron in lower mantle minerals: Implications to deep mantle geophysics and geochemistry. *Reviews of Geophysics* **51**, 244–275 (2013).
- Wang, Y. *et al.* Giant Pressure-Driven Lattice Collapse Coupled with Intermetallic Bonding and Spin-State Transition in Manganese Chalcogenides. *Angew. Chem. Int. Ed.* **10350**–10353 (2016).
- Murnaghan, F. D. The Compressibility of Media under Extreme Pressures. *Proc. Natl. Acad. Sci.* **30**, 244–247 (1944).
- Birch, F. Finite Elastic Strain of Cubic Crystals. *Phys. Rev.* **71**, 809–824 (1947).
- Santillán, J., Shim, S.-H., Shen, G. & Prakapenka, V. B. High-pressure phase transition in Mn_2O_3 : Application for the crystal structure and preferred orientation of the CaIrO_3 type. *Geophys. Res. Lett.* **33**, L15307 (2006).
- Yamanaka, T., Nagai, T., Okada, T. & Fukuda, T. Structure change of Mn_2O_3 under high pressure and pressure-induced transition. *Z. Kristallogr.* **220**, 938–945 (2005).
- Hong, F. *et al.* Pressure-induced isostructural transition in a distorted perovskite via octahedron reconfiguration. *Appl. Phys. Lett.* **109**, 241904 (2016).
- Yue, B. *et al.* Deformation Behavior across the Zircon-Scheelite Phase Transition. *Phys. Rev. Lett.* **117**, 135701 (2016).
- Hong, F. *et al.* High pressure polymorphs and amorphization of upconversion host material $\text{NaY}(\text{WO}_4)_2$. *Appl. Phys. Lett.* **109**, 041907 (2016).
- Hong, F. *et al.* Pressure-enhanced light emission and its structural origin in Er:GdVO_4 . *Appl. Phys. Lett.* **110**, 021903 (2017).
- Shen, Y., Kumar, R. S., Pravica, M. & Nicol, M. F. Characteristics of silicone fluid as a pressure transmitting medium in diamond anvil cells. *Rev. Sci. Instrum.* **75**, 4450–4454 (2004).
- Klotz, S., Chervin, J. C., Munsch, P. & Marchand, G. L. Hydrostatic limits of 11 pressure transmitting media. *J. Phys. D: Appl. Phys.* **42**, 075413 (2009).
- Erements, M. I. *et al.* Electrical Conductivity of Xenon at Megabar Pressures. *Phys. Rev. Lett.* **85**, 2797–2800 (2000).

Acknowledgements

The authors acknowledge support from the NSAF (Grant No: U1530402). F. H. and B.B. Y. acknowledge the usage of beam time at Beamline 10XU in Spring-8 (PN: 2014B1254) and beam time at 1.4.4 in the Advanced Light Source at Lawrence Berkeley National Laboratory. F. H. acknowledges Dr. Feng Ke for the kind discussion of the electrical measurement under high pressure. All authors thank Freyja O'Toole for her careful revision of the manuscript.

Author Contributions

F.H. and B.B.Y. conceived and designed the experiments. F.H., B.B.Y. and N.H. performed the experimental measurements. F.H., B.B.Y., Z.X.L., and B.C. analyzed the data and wrote the paper. All authors discussed the results and commented on the manuscript.

Additional Information

Supplementary information accompanies this paper at <http://www.nature.com/srep>

Competing Interests: The authors declare no competing financial interests.

How to cite this article: Hong, F. *et al.* Significant improvement in Mn_2O_3 transition metal oxide electrical conductivity via high pressure. *Sci. Rep.* 7, 44078; doi: 10.1038/srep44078 (2017).

Publisher's note: Springer Nature remains neutral with regard to jurisdictional claims in published maps and institutional affiliations.



This work is licensed under a Creative Commons Attribution 4.0 International License. The images or other third party material in this article are included in the article's Creative Commons license, unless indicated otherwise in the credit line; if the material is not included under the Creative Commons license, users will need to obtain permission from the license holder to reproduce the material. To view a copy of this license, visit <http://creativecommons.org/licenses/by/4.0/>

© The Author(s) 2017